Tungsten (2023) 5:50–66
https://doi.org/10.1007/s42864-021-00132-3

Tungsten
www.springer.com/42864

REVIEW PAPER

Application of high-pressure technology in exploring mechanical properties of high-entropy alloys

Shu-Cong Li[1] · Qing-Lin Wang[1] · Yu Yao[1] · Dan-Dan Sang[1] · Hai-Wa Zhang[1] · Guo-Zhao Zhang[1] · Cong Wang[2] · Cai-Long Liu[1]

Received: 12 October 2021 / Revised: 20 November 2021 / Accepted: 22 November 2021 / Published online: 1 February 2022

Abstract
In recent years, high-entropy alloys (HEAs) have developed a lot as the new style of materials, which have become a research focus in the materials fields. It breaks the normal procedure of traditional alloy design (based on one/two elements as the main component, and adds some other elements to improve the microstructure and required related performance of the alloy), and consists of five or more equal or nearly equal elements, with multiple principal elements. Therefore, HEAs have many excellent mechanical properties compared with traditional alloys, which have aroused great research interest of researchers. The rapid development of high-pressure technology makes it a powerful tool to modulate the structures of HEAs, and brings new chance for the study and optimization of mechanical properties of HEAs. In this paper, the application of high-pressure technology in exploring and improving the mechanical properties of HEAs is reviewed, which could deepen the understanding of high-pressure technology and provide a new avenue for further exploration of HEAs' mechanical properties.

Keywords High-entropy alloys · Mechanical properties · High-pressure torsion · High-pressure · Diamond anvil cells

1 Introduction

As a class of new materials, high-entropy alloys (HEAs) have properties that traditional materials do not have due to their unique design concepts [1–3], such as high strength, high ductility, high hardness, superplasticity, superconductivity, and other excellent properties (as shown in Fig. 1). The part of HEAs [4] represents a four-dimensional (4D) quinary phase diagram and the Co–Cr–Fe–Mn–Ni phase diagram. For the high strength part, the above one [5] shows the strain distribution after the tensile test, while the below one [6] provides the elemental distribution map and selected area electron diffraction (SAED) pattern about $(CoCrFeNi)_{94}Ti_2Al_4$ HEA after 2 turn high-pressure torsion (HPT). The part of high hardness [7] shows the {111} X-ray diffraction (XRD) pole figures of sample after 1/4 and 1 turn HPT. The superconductivity part [8] reveals the pressure dependence of electronic density of states and electrical resistivity of the as-cast TiZrHfNb HEA under different pressures. The part of superplasticity [9] shows the electron backscatter diffraction (EBSD)-inverse pole figure (IPF) map and the corresponding phase map of annealed sample. Therefore, HEAs have attracted extensive attention from researchers [10–14]. At the same time, HEA's multi-major element concept provides a great impetus for the development of new alloys for advanced applications [4, 15]. The progress of high-pressure experimental technology has directly promoted the research in the field of HEAs [16]. At present, the main high-pressure methods used for studying the properties of HEAs are HPT technology and diamond anvil cells (DAC). In this paper, the mechanical properties of HEAs under high pressure are reviewed, and the potential properties of HEAs under high pressure are prospected.

✉ Qing-Lin Wang
wangqinglin@lcu.edu.cn

✉ Cong Wang
wangcongphysics@mail.buct.edu.cn

✉ Cai-Long Liu
cailong_liu@jlu.edu.cn

[1] Shandong Key Laboratory of Optical Communication Science and Technology, School of Physics Science & Information Technology, Liaocheng University, Liaocheng 252059, China

[2] College of Mathematics and Physics, Beijing University of Chemical Technology, Beijing 100029, China

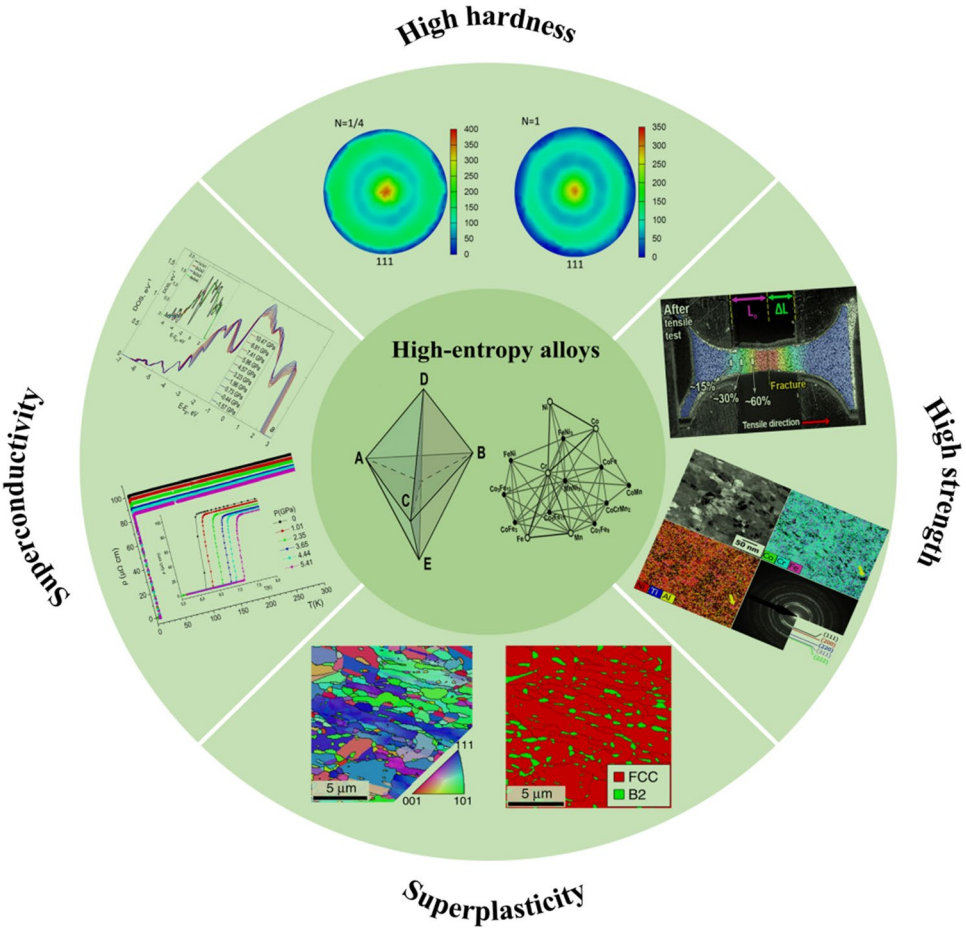

Fig. 1 Some excellent properties of HEAs. The part of HEAs is reproduced with permission from Ref. [4]. Copyright 2017 Elsevier. The above part of high strength is reproduced with permission from Ref. [5]. Copyright 2021 Elsevier. The below part of high strength is reproduced with permission from Ref. [6]. Copyright 2019 Elsevier. The part of high hardness is reproduced with permission from Ref. [7]. Copyright 2019 Elsevier. The part of superconductivity is reproduced with permission from Ref. [8]. Copyright 2022 Elsevier. The part of superplasticity is reproduced with permission from Ref. [9]. Copyright 2020 Springer Nature

2 HEAs

The earliest research on HEAs can be traced back to the proposal of crystal multi-major element alloys (MPEAS) in 1970 [11]. After a series of developments, the HEAs were systematically introduced in several works published in 2004 [3, 17–20]. HEA is an equiatomic and multi-element system, and there are many definitions of HEAs [21]. Two more representative definitions were based on component and entropy.

Defined by component, the HEA is an alloy consisting of five or more metal elements in tantamount or approximately tantamount quantities. The concentration of major elements should be between 5 and 35 at.%, and trace elements can be contained, but the concentration of minor elements should be less than 5 at.% [11, 20, 22]. Trace elements can change the properties of matrix HEAs, so different trace elements can produce different properties, thus expanding the HEA's system. However, this combination-based definition is only specified and stated in the dimension of elements, without mentioning the effect of entropy, which is not conducive to further understanding of the properties of HEAs.

From the viewpoint of entropy, the HEA is defined as the alloy whose mixed configuration entropy (ΔS_{mix}) of the n-element equiatomic alloy changes from elemental state to random solution state (ideal state or regular state) [22]. ΔS_{mix} can be calculated according to Boltzmann's hypothesis

$$\Delta S_{mix} = R\ln n, \tag{1}$$

where R is the gas constant (8.31 $JK^{-1}\cdot mol^{-1}$) and n is the number of elements for equimolar alloys. The calculation result of Eq. (1) is shown in Fig. 2a.

According to the mixing entropy in the random solution state [22], alloy can be roughly divided into the following categories, (i) low entropy alloys, (ii) medium entropy alloys, and (iii) high-entropy alloys, as shown in Fig. 2b.

2.1 Four core effects

For the sake of further understanding the properties of HEAs, Yeh [22] summarized four core effects of HEAs, which favored the excellent properties of HEAs: (1) high-entropy effects; (2) sluggish diffusion; (3) severe lattice distortion; and (4) cocktail effects.

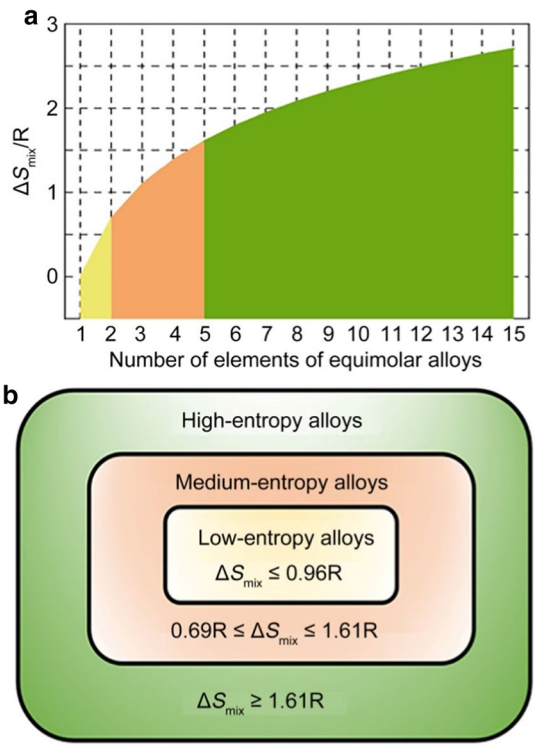

Fig. 2 **a** Variation of the $\Delta S_{mix}/R$ with the number of elements in equiatomic alloy; **b** the classified alloys according to the mixing entropy in the random solution states

2.1.1 High-entropy effect

For the HEAs, high-entropy effect is the most basic characteristic. In simple terms, because of the high mixing entropy of the HEAs, it does not form a complex and fragile microstructure inside, but only consists of several solid solution phases or even a single phase. It can also be understood that the high entropy favors the stable high-entropy phase, namely the solid solution phase, instead of the intermetallic phase [22–26].

2.1.2 Sluggish diffusion effect

The sluggish diffusion effect is a significant reason why HEAs have many excellent properties [27], which leads to excellent high-temperature strength [28, 29]. In short, the diffusion and phase transition dynamics of HEAs are slower than those of traditional alloys [25, 30].

2.1.3 Severe lattice-distortion effect

Because the size of different elements in HEAs is imparity in many cases, this size difference will bring about serious lattice distortion and will also affect the properties of HEAs [22, 25]. As shown in Fig. 3, the different dimensions of the elements cause severe lattice distortion.

2.1.4 Cocktail effect

Ranganathan [31] was the initial person to propose the cocktail effect of alloys. The original intention was "pleasant mixture" to describe the characteristics of trace elements in alloys that regulated their properties. Later, it meant a synergistic mixture that the final result was unpredictable and larger than the sum of its parts. The cocktail effect of HEAs is that their properties are not only the superposition of the

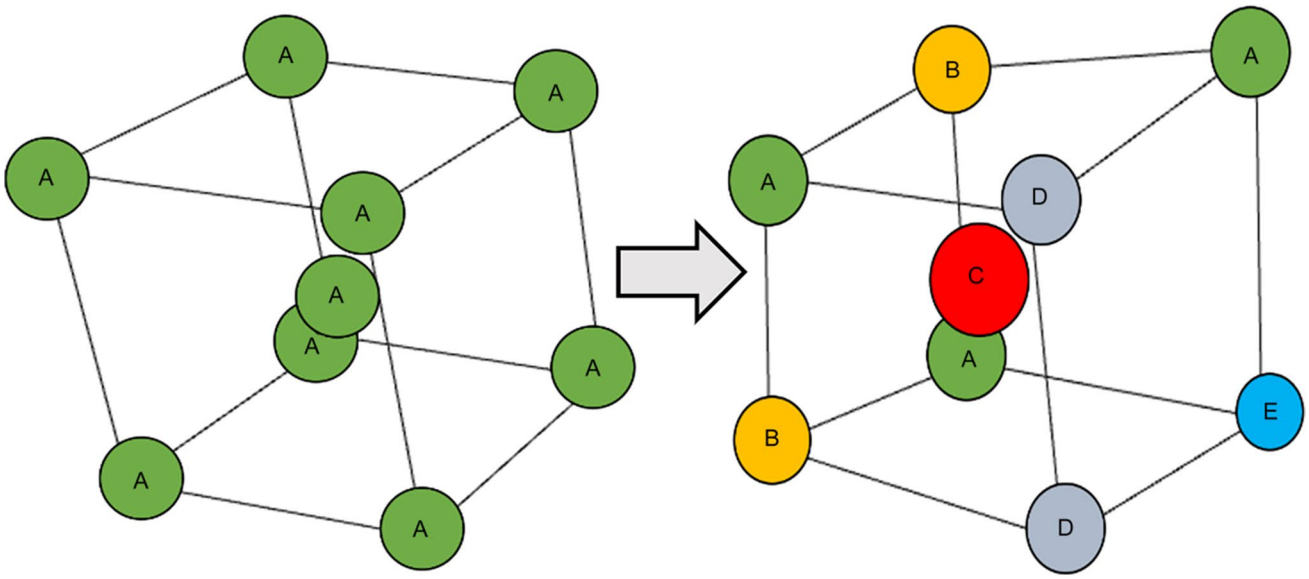

Fig. 3 Schematic illustration of lattice distortion

properties of each element, but also related to the interaction between elements [20, 23].

3 High-pressure technology

With the rapid development of high-pressure technology, it provides new possibilities for material research [32, 33]. At present, the main methods to realize high pressure in laboratory are HPT technology and diamond anvil cells.

In 1935, Bridgman [34] first proposed HPT technology. The working principle is shown in Fig. 4a. HPT is a severe plastic deformation (SPD) technique in which samples are subjected to torsional shear strain under high hydrostatic pressure [35]. By placing the sample between two anvils, when the external force drives the relative rotation of the two anvils, the friction between the sample and the anvil drives the rotation of the sample, causing the shear deformation of the sample. Many materials can withstand large shear strains without failure through HPT treatments [34, 36, 37].

In 1955, Bundy [38] synthesized diamond with high-pressure and high-temperature technology, making it possible for high-pressure technology to be widely used in material research. The first diamond anvil cell was made in 1958 with the tools at hand [39]. The diamond anvil structure is shown in Fig. 4b.

The DAC is composed of two opposite diamond anvils. By turning external screws, the sample is squeezed to generate hydrostatic/non-hydrostatic pressure [16, 33, 40]. In 1977, Buras et al. [41] first combined synchrotron radiation XRD method with DAC, which promoted the development of high-pressure technology.

4 Mechanical properties of HEAs under HPT

4.1 Change in hardness

High-pressure treatment can refine the grain size of HEAs and improve their hardness. For example, it can affect a sample by changing the hardness and softness of its phase. Stepanov et al. [42] made the $AlNbTiVZr_{0.5}$ HEA disk rotate 0.25, 0.5, 1, and 5 rotations at room temperature, 8 GPa pressure, and 0.5 r·min^{-1}, respectively. The nano-hardness of single phase indicated that the increase of hardness was due to the structural refinement of B2 phase. At the same time, the Laves phase became softer during HPT processing. As shown in Fig. 5a, the microhardness increased with the increasing number of turns and the increasing distance from the center of the disk until it reached the saturation state. After five HPT rotations, the microhardness of the sample increased from 550 HV to a maximum of 665 HV.

Meanwhile, the change of strain path also affects the hardness of HEAs. Sonkusare et al. [43] performed monochromatic and cyclic HPT on a CoCuFeMnNi HEA disk at room temperature and 5 GPa. Five forward and reverse cyclic single-step and multi-step torsions at 100° and 360° were performed, respectively. It was shown that the microhardness of the HPT-treated sample was significantly higher than that of the annealed sample. Figure 5b visually shows the change in hardness for the entire quarter of the disk subjected to HPT. The periphery of the 100° cyclic HPT sample exhibited the highest hardness due to the change of strain path, and significant grain refinement occurred with the evolution of complex dislocation substructure. The low hardness of HPT alloy with 360° cycle was caused by the unstable dislocation substructure which promoted grain boundary migration and grain growth. In Fig. 5c, the crystal

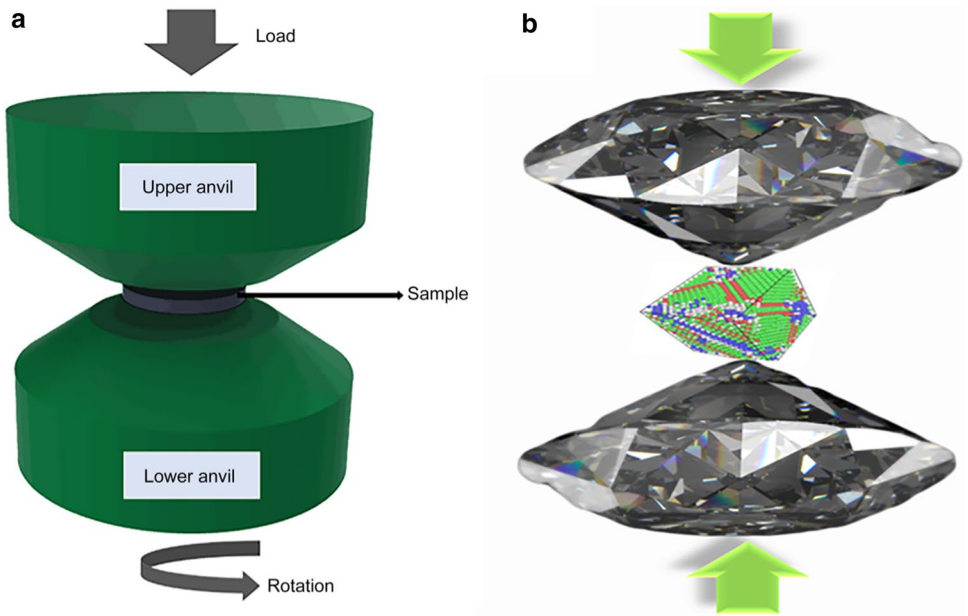

Fig. 4 **a** Schematic diagram of high-pressure torsion and **b** diamond anvil cells

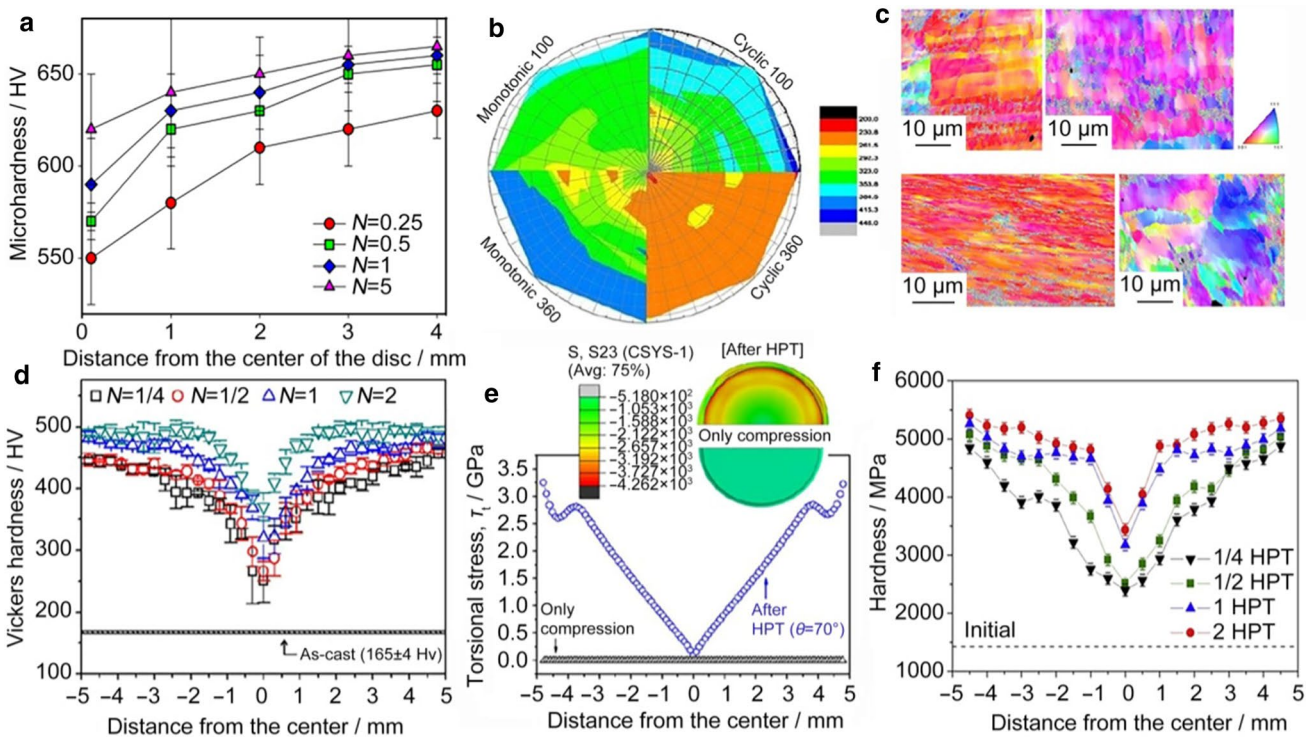

Fig. 5 **a** The relationship between the microhardness of $AlNbTiVZr_{0.5}$ alloy and the distance from the center of disk after different HPT turns (N). Reproduced with permission from Ref. [42]. Copyright 2018 Elsevier. **b** Two-dimensional contour map of hardness of samples treated with different HPT; **c** IPF maps of samples with monotonic 100°, cyclic 100°, monotonic 360°, and cyclic 360° HPT-treated. Reproduced with permission from Ref. [43]. Copyright 2019 Springer Nature. **d** The Vickers hardness of nanocrystals CoCrFeNiMn after different HPT treatment as a function of the distance from the center of the disk; **e** simulation diagram of nanocrystalline CoCrFeNiMn torsional stress with disk center distance after compression and 1/5 HPT treatment. The distribution of torsional stress on the surface of semicircular disk was shown in different colors. Reproduced with permission from Ref. [44]. Copyright 2015 Springer Nature. **f** The Vickers microhardness evolution of nanocrystalline CoCrFeMnNi as a function of center distance after 1/4, 1/2, 1, and 2 turns of HPT treatment. Reproduced with permission from Ref. [45]. Copyright 2017 Elsevier

orientation or IPF map near the center of the HPT-processed disk showed that there was a large color gradient inside the grains, indicating that there was an orientation gradient due to the dislocation activity.

HPT can be used to improve the hardness of nanocrystalline HEAs. Lee et al. [44] performed 1/4, 1/2, 1, and 2 turns of nanocrystalline CoCrFeNiMn HEA disks at room temperature, 6.0 GPa pressure, and 1 r·min^{-1}. The Vickers hardness test of the samples after treatment is shown in Fig. 5d. HPT treatment significantly improved the hardness of the samples, and the grain refinement degree was positively correlated. The nanocrystalline structure was also obvious in the early stages of HPT processing due to the severe torsional stresses which strengthen the atomic diffusion. At the same time, the finite-element analysis simulation of the radial variation of 1/5 HPT-treated samples from the center of the disk was carried out. In Fig. 5e, finite-element simulation estimated the variation of torsional stress τ_t from the center of the disk along the radial direction. The simulated rotation angle was 70°, which was close to 1/5 HPT. Different stresses were represented on the disk in different colors. As the distance from the center increases, τ_t increased significantly and exhibited maximum stress of 3.26 GPa at the edge.

Heczel et al. [45] conducted HPT tests at room temperature, 3.0 GPa pressure, and 1 r·min^{-1} on nanocrystalline CoCrFeMnNi with 1/4, 1/2, 1, and 2 turns, respectively. The hardness measured along the disk diameter after HPT treatment is shown in Fig. 5f. At 1/4 turn, the hardness gradient along the radius of the disk was large. At 1/2 turn tight, there was mild hardening in the center and periphery. It was also observed that the hardness of the middle area increased greatly from 1/2 turn to 1 turn. It was observed that the hardness changed little during the process of 1–2 turns, and a higher number of turns might produce the completed saturation of hardness. The maximum hardness of the outer disk reached 5.38 GPa after two turns. Basically, the smaller the grain size, the greater the hardness; the greater the change of grain size, the greater the degree of hardness improvement. Not only grain refinement but also twins were taken shape in the grain. The EBSD images (Fig. 6a, b) of the 1 HPT-treated sample

showed that twins with an average spacing of 3 μm were formed in the crystal.

HPT can also be used to improve the hardness of nanostructured dual-phase HEAs. Edalati et al. [46] treated nanostructured dual-phase AlCrFeCoNiN HEA with $N = 1/16$, 1/4, 1, and 4 cycles of HPT at 300 K temperature, 6 GPa pressure, and 1 r·min^{-1} rotation speed, respectively. The measurement of microhardness of samples treated under different conditions (Fig. 6c) showed that after 4 cycles of HPT treatment, the sample reached the ultra-high hardness of 1030 HV. This was caused by nanoparticles with high lattice distortion, interface formation dislocation generation, and average size of 10 nm. Meanwhile, scanning electron microscope–energy-dispersive X-ray spectroscopy (SEM–EDS) analysis was performed on the initial sample, 1/4 and 4 laps of HPT samples to detect the distribution of various elements, and the results were shown in Fig. 6d–f. It should be noted that after HPT treatment, the composition of the phase did not change, but each phase was mixed, and it was obvious with the increase of HPT treatment winding number.

The saturation state of the material can be investigated by the HPT effect due to the balance between hardening and softening of the material. Yu et al. [47] treated $Al_{0.1}$CoCrFeNi with HPT for 1 and 2 turns at a speed of 1 r·min^{-1} and a pressure of 6 GPa. Vickers microhardness was measured along the radius of the treated samples. The results are shown in Fig. 6g. Under hot-isostatic pressing, the microhardness increased from 135 HV to about 482 HV, and increased to saturation with the increase of strain (from center to edge). At the same time, the results showed that the edge hardness of the sample was about 482 HV, which reached the balance of softening and hardening, and the material reached the saturation state.

HPT is a rapid synthesis method for preparing HEAs nanocomposites [48]. Taheriniya et al. [49] connected two single-phase equiatomic bcc-HfNbTaTiZr and fcc-CoCrFeMnNi HEAs disks by HPT method. The connection was achieved by rotating 5, 10, 15, and 20 times at an ambient temperature and hydrostatic pressure of 9 GPa, and Vickers microhardness measurements were performed on the treated samples (as shown in Fig. 7a). The results showed that the microstructure of the newly formed nanocomposites was refined and the hardness was increased by 5–20 revolution. Under the same conditions, the hardness of co-deformed double bcc–fcc nanocomposites exceeded that of the two single-phase materials. Figure 7b, c shows high-resolution and high-speed nanoindentation patterns obtained by continuous stiffness measurement (CSM) method from the edge

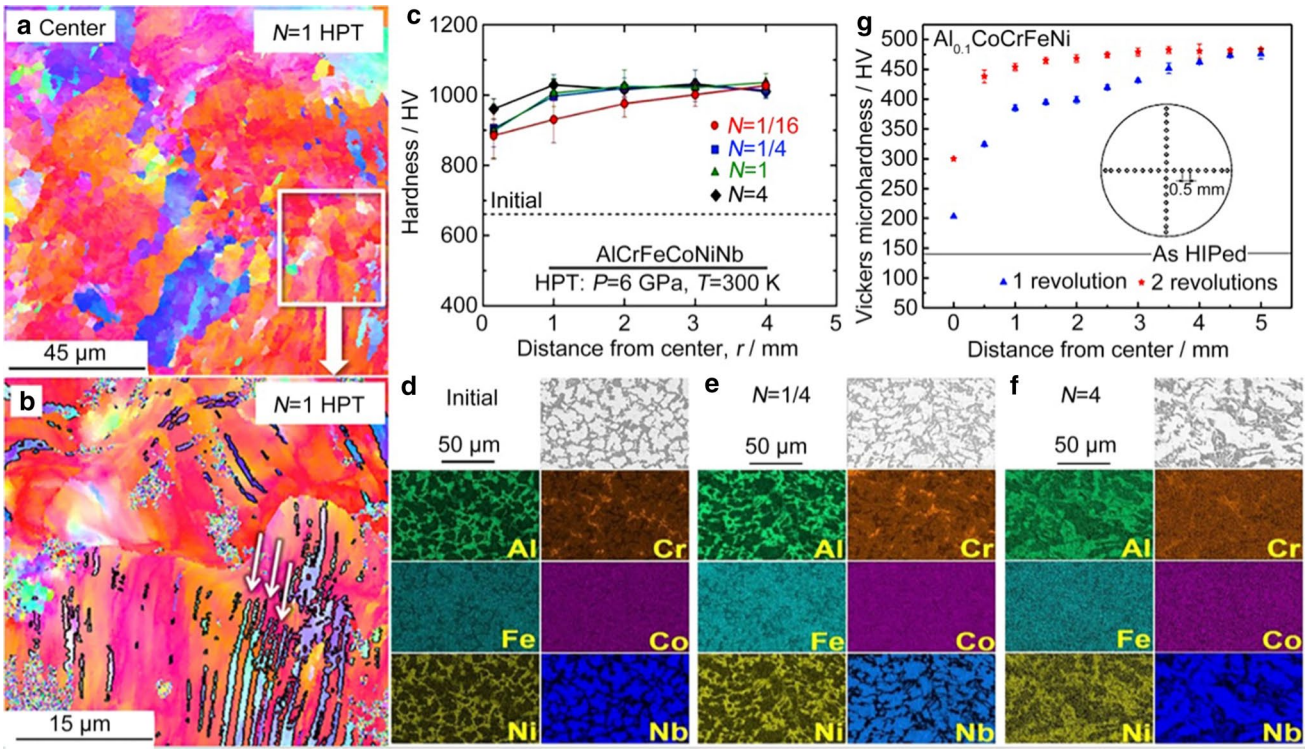

Fig. 6 **a, b** EBSD images of nanocrystalline CoCrFeMnNi sample disk center after 1 turn of HPT, and further magnification of part of the region. Reproduced with permission from Ref. [45]. Copyright 2017 Elsevier. **c** Vickers microhardness versus distance from disk center; SEM–EDS analysis of **d** the initial AlCrFeCoNiNb high entropy alloy and **e** 1/4 turns HPT-treated and **f** 4 turns HPT-treated samples to check the element distribution map. Reproduced with permission from Ref. [46]. Copyright 2021 Elsevier. **g** The Vickers microhardness of $Al_{0.1}$CoCrFeNi at 6 GPa after 1 and 2 cycles of hot-isostatic pressed (HIPed) and HPT treatments as a function of the distance from the center of the disk. Reproduced with permission from Ref. [47]. Copyright 2016 Elsevier

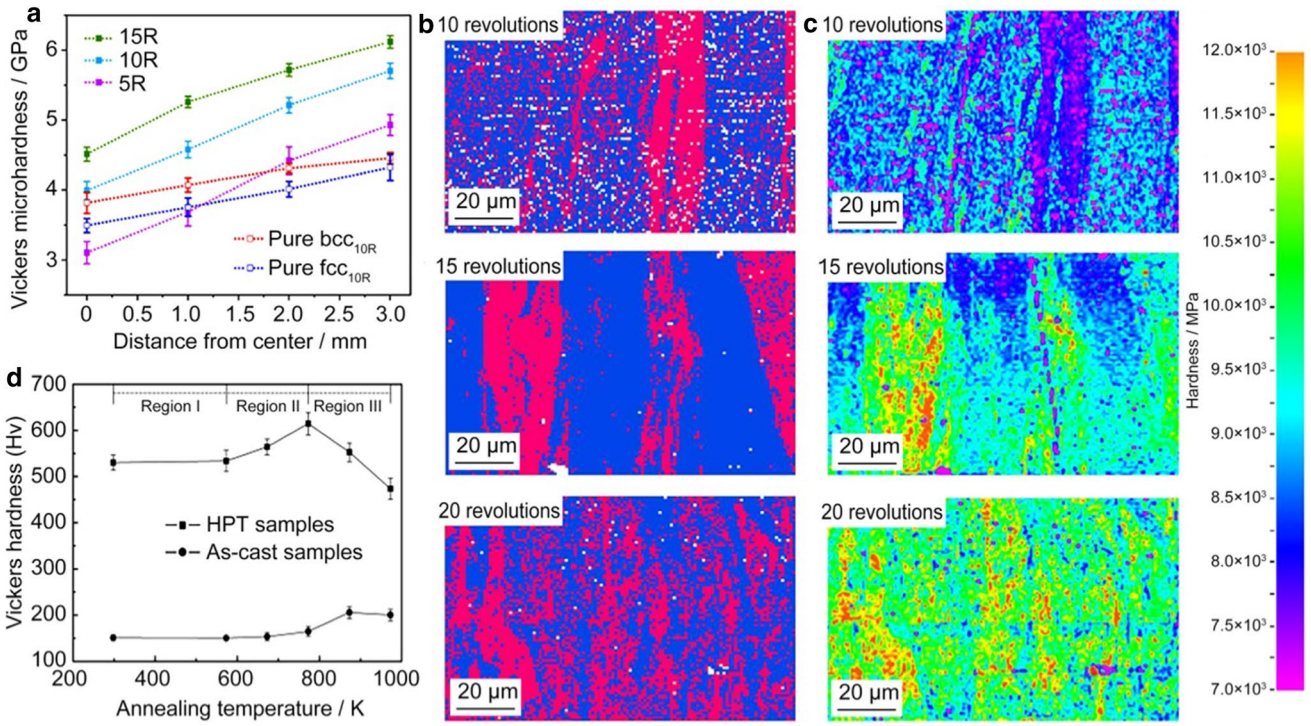

Fig. 7 **a** Relationship between dual-phase HEAs microhardness and center distance after 5, 10, and 15 HPT treatments. The Vickers microhardness curves of the single-phase fcc and bcc alloys were given; high-resolution and high-speed nanoindentation images of dual-phase HEAs at 10, 15, and 20 revolutions for **b** cluster diagram of average hardness of two different phases and for **c** hardness intensity distribution in two phases. Reproduced with permission from Ref. [49]. Copyright 2021 Elsevier. **d** The variation of as-cast Vickers hardness and HPT HEA with annealing temperature. Reproduced with permission from Ref. [50]. Copyright 2015 Elsevier

of HPT deformed samples after 10, 15, and 20 revolutions. The hardness distributions of different phases and phase boundaries as a function of deformation were summarized. Figure 7a–c jointly confirms that the significant increase in hardness of mixed HEAs was related to the non-uniform co-deformation of the two-phase lamellar HEA composite.

The combination of HPT and thermal annealing treatment is a method to further improve the hardness of HEAs. Tang et al. [50] treated $Al_{0.3}$CoCrFeNi samples with HPT at 8 r·min^{-1} at room temperature and 6.0 GPa, resulting in the steady-state grain size and uniform microstructure of the samples. Then, the untreated samples and HPT samples were annealed at different temperatures, and the microhardness was measured, respectively. As shown in Fig. 7d, the maximum hardness of the HPT sample was about 4 times that of the original hardness of as-cast HEA, and the increase of hardness was mainly caused by the grain refinement to the nanometer range. In addition, during the annealing process, HPT samples formed hard secondary phase (ordered annealing bcc structure rich in Al and Ni), which further improved the hardness.

HPT can also be applied to the synthesis of dense HEAs. Elemental powders of Co, Cr, Fe, Mn, and Ni were mixed in argon with a medium molar ratio by Kilmametov et al. [51]. Then, the mixed powders were treated with HPT, respectively. The microhardness test results are shown in Fig. 8a. Due to the uneven distribution of elements, incomplete phase formation, or low material density, the hardness in the central region of the sample increased abnormally after 1 rotation. After 10 rotations, the maximum hardness of 7.3 GPa was measured at the edge of the sample. At the same time, the uniformity of elements at nanometer scale was analyzed by atom probe tomography (APT) and the oxidation particles were studied. Figure 8b shows the reconstruction of Co, Cr, Fe, Mn, and Ni as well as the distribution of CrO and O ions at the tip. The results showed that the concentration of the main elements along the tip did not fluctuate much and a Mn-enriched grain boundary could be authenticated during the reconstruction process. The distribution of CrO and O could reveal the formation of several nano-sized Cr oxides.

HPT combined with annealing treatment can break through the saturation state of the material and further improve the hardness of the material. Schuh et al. [52] treated CoCrFeMnNi HEA with HPT for 1/4, 1, and 5 turns at 7.8 GPa pressure, 0.2 r·min^{-1}, and room temperature. The microhardness was significantly improved. Then, the samples treated with 5 cycles were annealed at disparate

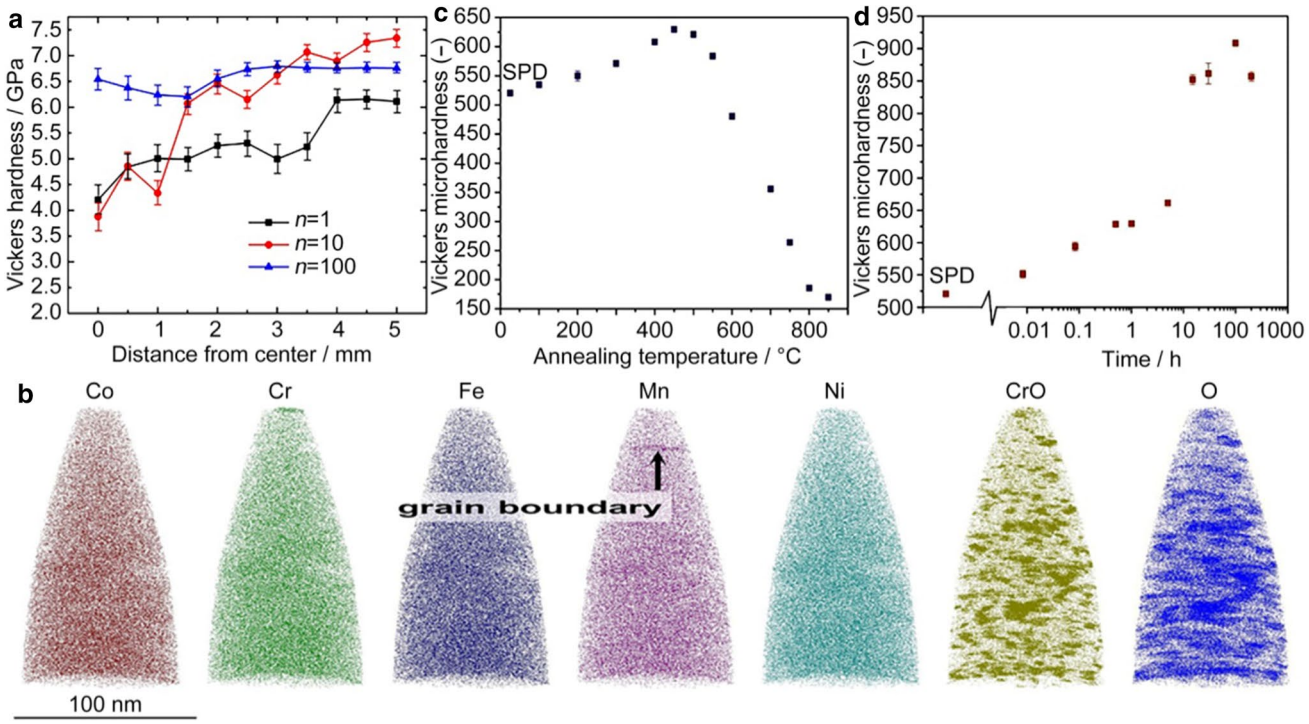

Fig. 8 **a** Relationship between microhardness and distance from center of CoCrFeMnNi treated with 1, 10, and 100 turns of HPT; **b** distribution of the atoms in the tip atom. Mn-enriched grain boundary is marked during Mn reconstruction. Both the detected CrO and O ions are displayed. Only 1% of the other ions were extracted from the probe. Reproduced with permission from Ref. [51]. Copyright 2019 Elsevier. **c** Vickers hardness of isochronous (1 h) treated samples at different annealing temperatures; **d** Vickers hardness of samples treated for unequal time at the same annealing temperature (450 °C). Reproduced with permission from Ref. [52]. Copyright 2015 Elsevier

temperatures. The results are shown in Fig. 8c. At 0–500 °C, the microhardness increased significantly even in the saturated state. The 5 HPT-treated samples were then isothermally treated at 450 °C for up to 200 h. As shown in Fig. 8d, the hardness continued to increase from the SPD state to a peak of 910 HV after 100 h of annealing, and then began to decline again. To correlate hardness variations with microstructure, 3-dimensional (3D)-APT treatment was performed on samples annealed at 450 °C, and the results are shown in Fig. 9a, b. The volume fraction increased obviously at 1 h. At 15 h, an additional phase mainly composed of Fe and Co is formed, and the volume fraction of the first two phases further increases. With the extension of annealing time, the composition of Mn, Ni phase remained unchanged and the content of Cr phase increased. After that, the content of each phase continued to change, but due to the high brittleness of the material, the experiment could not be continued, so it needs to be further studied.

4.2 Changes in superplasticity

Superplasticity is the extreme plastic deformation of fine-grained materials (up to 10 microns) at temperatures greater than 0.5 Tm (Tm is the melting temperature) with a tensile elongation of at least 400% [53, 54]. Shahmir et al. [55] applied HPT treatment to CoCrFeNiMn HEA for 5 turns at room temperature, 6.0 GPa pressure, and 1 r·min^{-1}. The grain size was refined to about 10 nm, and grain boundary sliding (GBS) occurred. The maximum total elongation at each temperature was measured, as shown in Fig. 9c. It could be seen that superplastic stretching (> 400%) occurred at 873 and 973 K, which proved the superplasticity of the material. Figure 10a–d shows the microstructure of the grip section and the gauge section of the specimens deformed at 973 K, at a strain rate of 1.0×10^{-3} s^{-1} and a stretch direction of tensile direction (TD). The arrows indicated the precipitates of the sample tested at 973 K.

Nguyen et al. [56] treated $V_{10}Cr_{15}Mn_5Fe_{35}Co_{10}Ni_{25}$ HEA with 5 turns of HPT at room temperature, 1 r·min^{-1}, and 6 GPa under applied pressure. The total elongation results are shown in Table 1. The material reached superplasticity and the temperature range for obtaining good elongation was larger. It could also be seen that the total elongation decreased with the decrease of strain rate, which was probably due to dynamic recovery process. The XRD patterns showed that there was a small fraction of σ phase in the samples tested at 973 K and 1073 K, and the formation of σ phase could be used as an obstacle to restrict the growth of fine grains and stabilize fine grains, thus contributing to the promotion of superplastic deformation. At a strain rate of

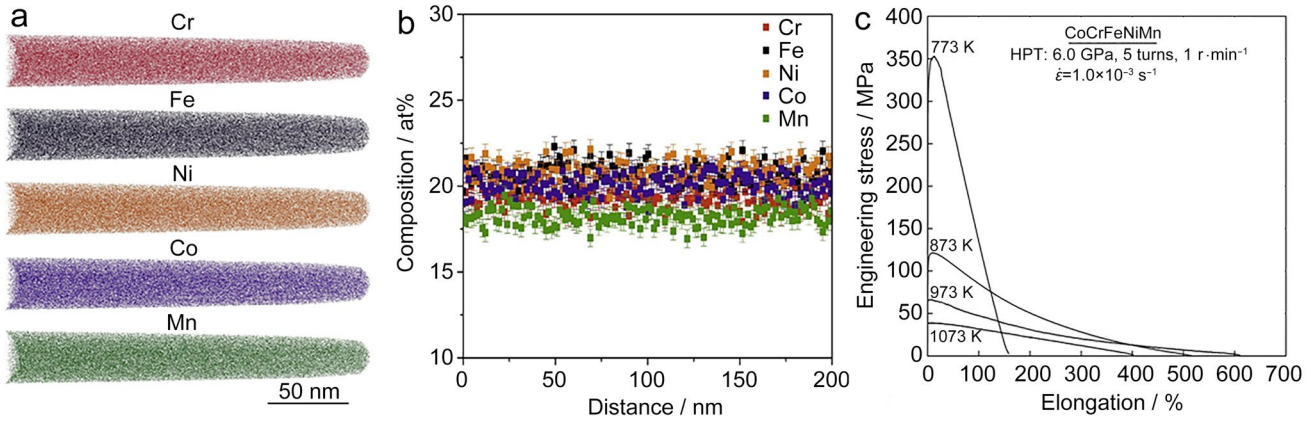

Fig. 9 **a** Chemical composition distribution on probe image; **b** Cr, Fe, Ni, Co, and Mn ion maps reconstructed by CoCrFeMnNi 3D-APT after severe plastic deformation. Reproduced with permission from Ref. [52]. Copyright 2015 Elsevier. **c** Engineering stress extension curves of CoCrFeNiMn HEA at 6 GPa, 1 r·min^{-1} and 1.0×10^{-3} s^{-1} strain rates at different temperatures. Reproduced with permission from Ref. [55]. Copyright 2017 Elsevier

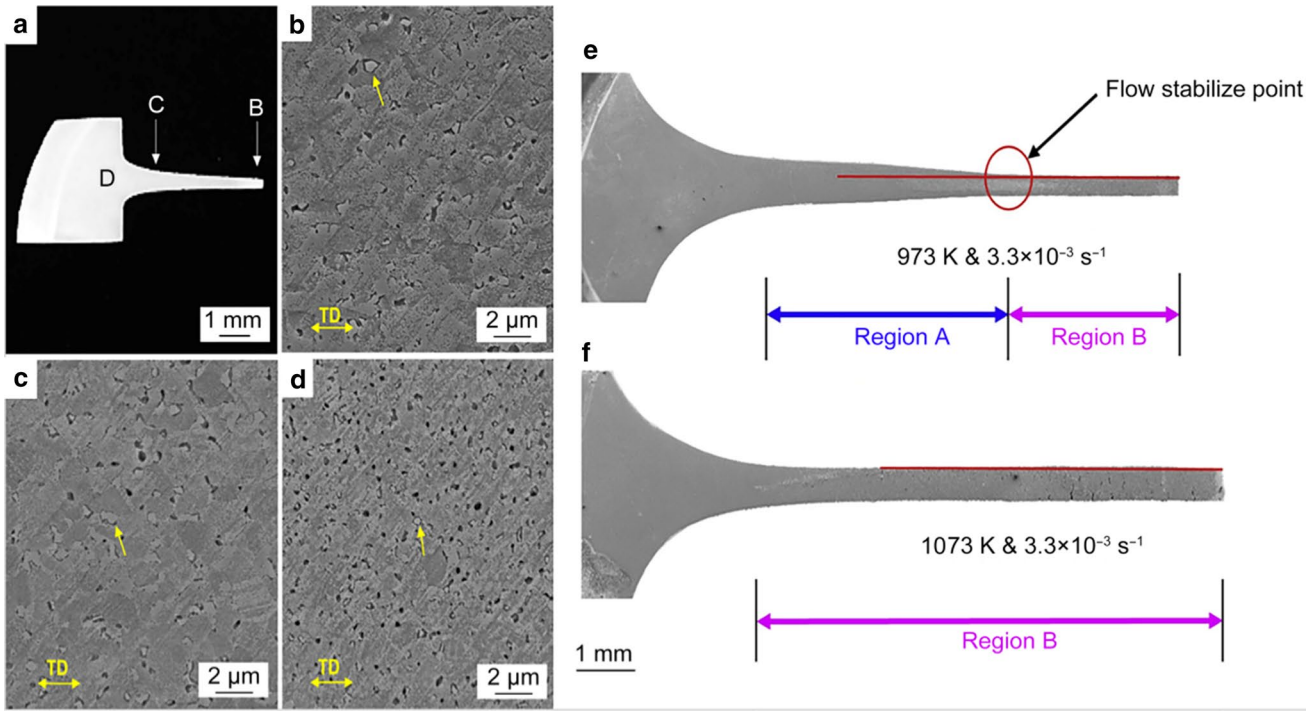

Fig. 10 **a** SEM images of 973 K samples with initial strain rate 1.0×10^{-3} s^{-1} and maximum elongation is 610%; **b–d** position corresponding to B, C and D in figure **a,** respectively. Arrows indicate precipitation and TD. Reproduced with permission from Ref. [55]. Copyright 2017 Elsevier. **e, f** SEM images of the fracture samples after tensile test at 1073 K, 3.3×10^{-3} s^{-1}, 700% elongation. Reproduced with permission from Ref. [56]. Copyright 2019 Elsevier

3.3×10^{-3} s^{-1}, the electron microscopy of 973 K and 1073 K samples from grip to fracture is shown in Fig. 10e, f. At 973 K, the width of the gauge decreased gradually to achieve quasi-uniform deformation, while at 1073 K, the width of the gauge was completely uniform.

Nguyen et al. [9] also achieved ultra-high strain rate superplasticity of nanostructured HEAs using HPT technology. An extremely rare high strain rate superplasticity (HSRS) has been achieved in high strength materials. The 10 mm $Al_9(CoCrFeMnNi)_{91}$ HEA disk was processed by HPT for 5 turns at room temperature, 6 GPa applied pressure, and 1 r·min^{-1}. The transmission electron microscope–electron dispersive X-ray spectroscopy (TEM–EDS) analysis of the sample (Fig. 11a) showed that sigma phase (rich in Cr) was

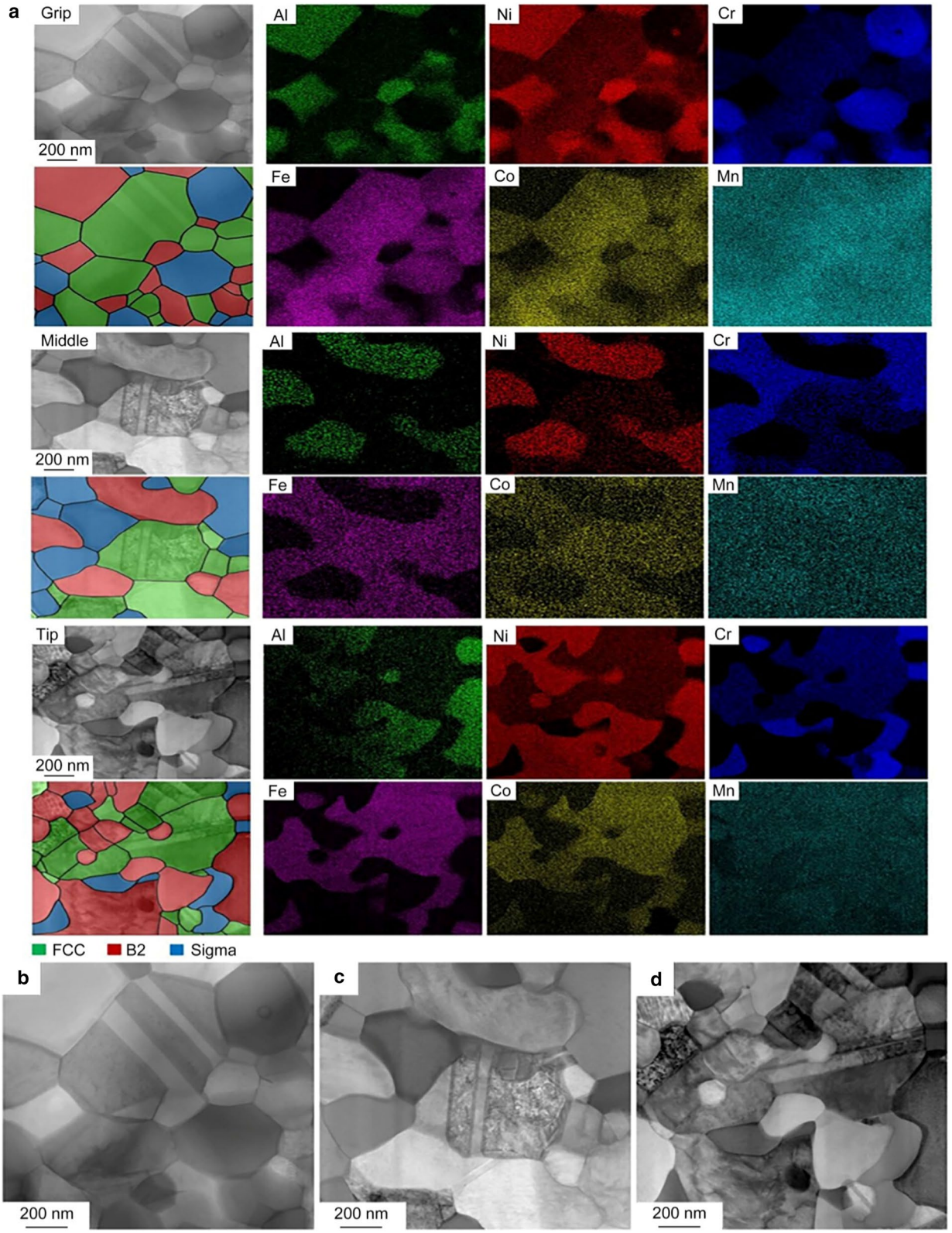

Fig. 11 **a** TEM-EDS images and phase diagrams of the grip, middle, and tip portions of the tested specimens were obtained at 1073 K and 5×10^{-2} s^{-1}; **b–d** $Al_9(CoCrFeMnNi)_{91}$ HEA scanning transmission electron microscope (STEM) images in the grip, middle, and tip. Reproduced with permission from Ref. [9]. Copyright 2020 Springer Nature

formed at 1073 K, and fcc and B2 phases were removed in the superplastic tests. Newly formed σ phase and B2 phase could prevent significant grain growth and facilitate grain boundary slip (GBS) with high strain rate sensitivity. In B2 and fcc phases, hole interconnections and dislocation activity were observed to be adapted to GBS. Fine grain size was associated with high strain rate sensitivity and GBS adaptation to plastic deformation. In other words, the combination of grain refinement induced by HPT and finite grain growth during thermoplastic deformation resulted in high strain rate superplasticity through GBS to which dislocation activity was suited. This kind of superplasticity under high strain rate greatly saved production time and promoted industrial production. Figure 11b–d shows the microstructure of the samples at different locations. It was found that there was no significant difference in grain size between the deformed and undeformed regions of the samples; thus, it can be concluded that there was almost no dynamic grain growth in the deformed region. The superplasticity test results are shown in Fig. 12a. The superplastic elongation of $Al_9(CoCrFeMnNi)_{91}$ HEA nanostructure was found to be 2000% of the original length at high strain rate (5×10^{-2} s^{-1}).

4.3 Good combination of ductility and strength

The balance between ductility and strength is a long-lasting problem in the field of materials research, and it is no exception in HEAs [57–59]. However, Pan et al. [60] recently solved this problem by controllable introduction of a novel gradient nano-scaled dislocation-cell structures in a stable single-phase *fcc*-$Al_{0.1}$CoCrFeNi HEA. Also, we found that HPT and annealing treatment of HEAs could effectively solve this problem [61].

Asghari-Rad et al. [5] treated CoCrFeMnNi samples with 4 cycles of HPT at 5 GPa pressure and 1 r·min^{-1}. The results in Fig. 12b showed that the tensile strength of the specimen was about 1867 MPa after HPT, but the elongation was low. The HPT disks were then annealed at 700 °C and 800 °C for 15 and 60 min in an argon atmosphere. After annealed processing, the toughness of samples was restored, but the tensile strength was decreased. The reason was that with the increase of annealing time and temperature, the dislocation density and grain growth caused by HPT decrease. Figure 12c–f shows EBSD-IPF maps of sample treated with HPT under various annealing conditions. The results showed that the average grain size of the sample reached 844 nm after annealing at 800 °C for 60 min. It increased with the increase of temperature and annealing time. When annealed at 700 °C, the σ particles produced in the samples would reduce the tensile strength. The final sample annealed at 800 °C for 60 min obtained a significant combination of strength and elongation.

Table 1 Elongation results and peak stresses of the HPT-processed $V_{10}Cr_{15}Mn_5Fe_{35}Co_{10}Ni_{25}$ HEA at strain rates and different temperatures. Reproduced with permission from Ref. [56]. Copyright 2019 Elsevier

Sample's order	Temperature (K)	Strain rate (s^{-1})	Elongation ε (%)	Peak stress δ (MPa)
	873	1.0×10^{-2}	130	248
1		5.0×10^{-3}	225	199
		1.0×10^{-3}	325	162
		5.0×10^{-4}	390	105
	973	1.0×10^{-2}	490	112
2		5.0×10^{-3}	480	90
3		3.3×10^{-3}	770	75
4		1.0×10^{-3}	650	65
5		5.0×10^{-4}	410	40
	1073	1.0×10^{-2}	580	64
6		5.0×10^{-3}	580	50
7		3.3×10^{-3}	700	40
		1.0×10^{-3}	630	25
8		5.0×10^{-4}	615	16

Shahmir et al. [62] treated the CoCrFeNiMn HEA with 1, 5, and 10 turns of HPT at room temperature and 6.0 GPa. The samples were then annealed at 473–1173 K for different times. The results are as shown in Table 2. The short-term annealing at 1073 K and 10 min could prevent the grain from growing and obtain high strength (830 MPa) and good plasticity.

Asghari-Rad et al. [63] processed $V_{10}Cr_{15}Mn_5Fe_{35}Co_{10}Ni_{25}$ HEA for five turns of HPT under quasi-constraint conditions, 25 °C, 6 GPa, and 1 r·min^{-1}. The samples were then annealed at 600–800 °C for 2–60 min. As shown in Fig. 12g, annealing at 700 °C for 10 min could obtain the best mechanical properties with high tensile strength and good elongation. Figure 13 shows the EBSD-IPF diagram of $V_{10}Cr_{15}Mn_5Fe_{35}Co_{10}Ni_{25}$ annealed at different temperatures and times. The results showed that the grain growth tended to be single at 700 °C with increasing annealing time. The annealing process at 800 °C for 60 min increased sharply the average grain size to ~ 1.4 μm.

5 Mechanical properties of HEAs under DAC

DAC is also commonly used in the study of HEAs. Using XRD and DAC techniques, Zhang et al. [64] studied the deformation behavior of MoNbTaVW HEA under compression conditions. Figure 14a shows the function images of azimuthally unrolled diffraction patterns of MoNbTaVW and W with direction angle before compression, under 5 GPa–20 GPa pressure and after pressure relief. At 5 GPa,

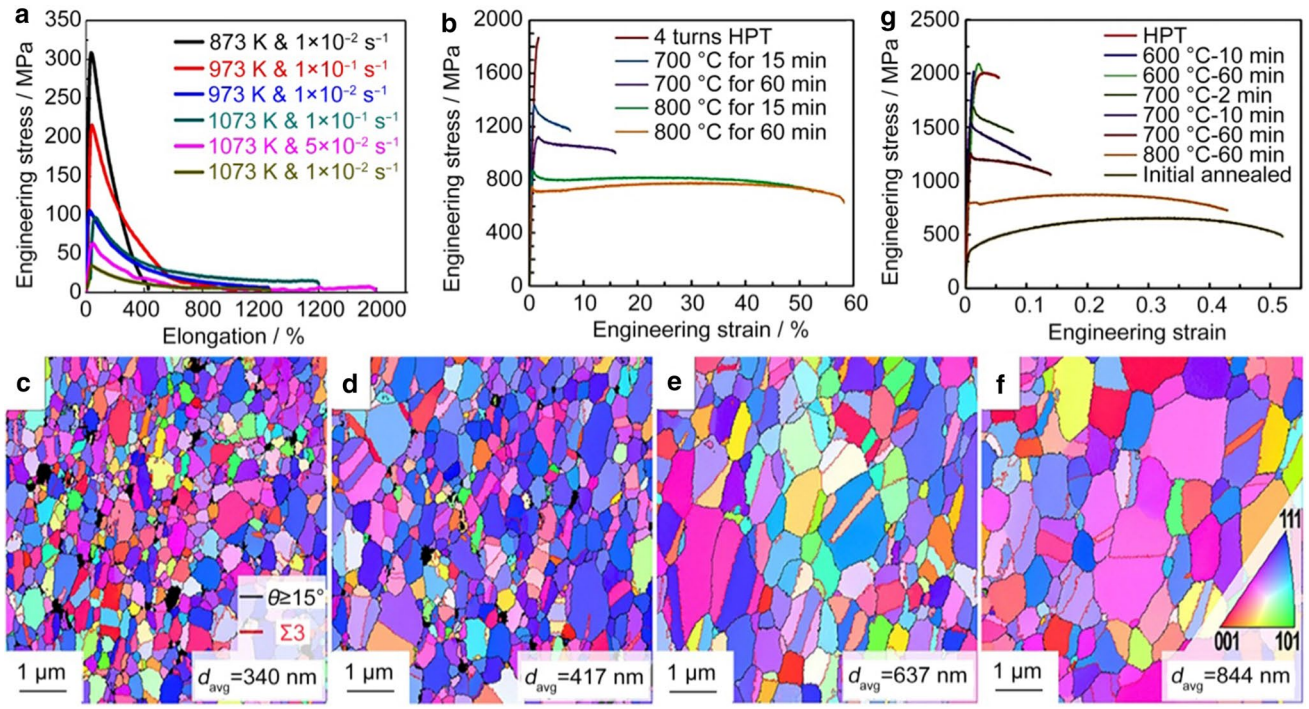

Fig. 12 **a** Engineering stress–strain curves of $Al_9(CoCrFeMnNi)_{91}$ in tensile tests at 873 K, 973 K and 1073 K and at $10^{-1} \sim 10^{-2}$ s^{-1}, respectively. Reproduced with permission from Ref. [9]. Copyright 2020 Springer Nature. **b** Engineering stress–strain curves of CoCrFeMnNi HEA powder billet after 4 HPT and post-HPT annealed; EBSD-IPF diagrams of the post-HPT annealed samples at **c** 700 °C for 15 min; **d** 700 °C for 60 min; **e** 800 °C for 15 min; **f** 800 °C for 60 min. Reproduced with permission from Ref. [5]. Copyright 2021 Elsevier. **g** Engineering stress–strain curves of $V_{10}Cr_{15}Mn_5Fe_{35}Co_{10}Ni_{25}$ HEA under different conditions. Reproduced with permission from Ref. [63]. Copyright 2020 Elsevier

both W and MoNbTaVW form in the bcc structure, resulting in strong lattice strain and texture. At 20 GPa, the diffraction peak of MoNbTaVW was much sharper than W, indicating that it had a larger lattice strain at high pressure. In the process of pressure relief, no new diffraction peaks were found, which confirmed the phase stability of W and MoNbTaVW. The XRD patterns (Fig. 14b) showed that MoNbTaVW had stronger resistance to high pressure than pure tungsten. It was founded that the active dislocation behavior was the main reason for the high strength of MoNbTaVW.

Also using XRD and DAC techniques, Zhang et al. [65] investigated the effect of dilute carbon doping on the mechanical properties of $Mo_{15}Nb_{20}Re_{15}Ta_{30}W_{20}$ HEA. The results show that high pressure/temperature promotes the formation of Ta_3C and Nb_3C carbides. The stable Ta_3C and Nb_3C carbides may further improved the mechanical properties of the Alloy. Table 3 indicates that low carbon concentration had small effect on the hardness of the alloy.

Zhang et al. [66] synthesized carbon-doped MoNbTaW alloy through ball milling. The performance of the alloy at 3.1 GPa and different temperatures was studied using the resistor-heating DAC. As shown in Fig. 15a, fcc carbides (TaC and NbC) and bcc (compositionally complex alloys) phases are present in the sample, and it is found that carbides are more easily obtained when high concentrations of C are added. XRD patterns of the samples (Fig. 15b) indicated good stability with increasing temperature from room

Table 2 Microhardness, yield strength (YS), ultimate tensile strength (UTS), and elongation (δ) of CoCrFeNiMn HEA before HPT and after post-deformation annealing (PDA) at 1073–1173 K for 10–60 min. Reproduced with permission from Ref. [62]. Copyright 2016 Elsevier

Annealing temperature (K)	Annealing time (min)	HV	YS (MPa)	UTS (MPa)	δ (%)
Homogenized	–	120	300	530	85
1073	10	290	680	830	65
	30	245	570	725	78
	60	220	530	680	80
1173	10	170	410	630	76
	30	155	390	610	80
	60	140	370	600	90

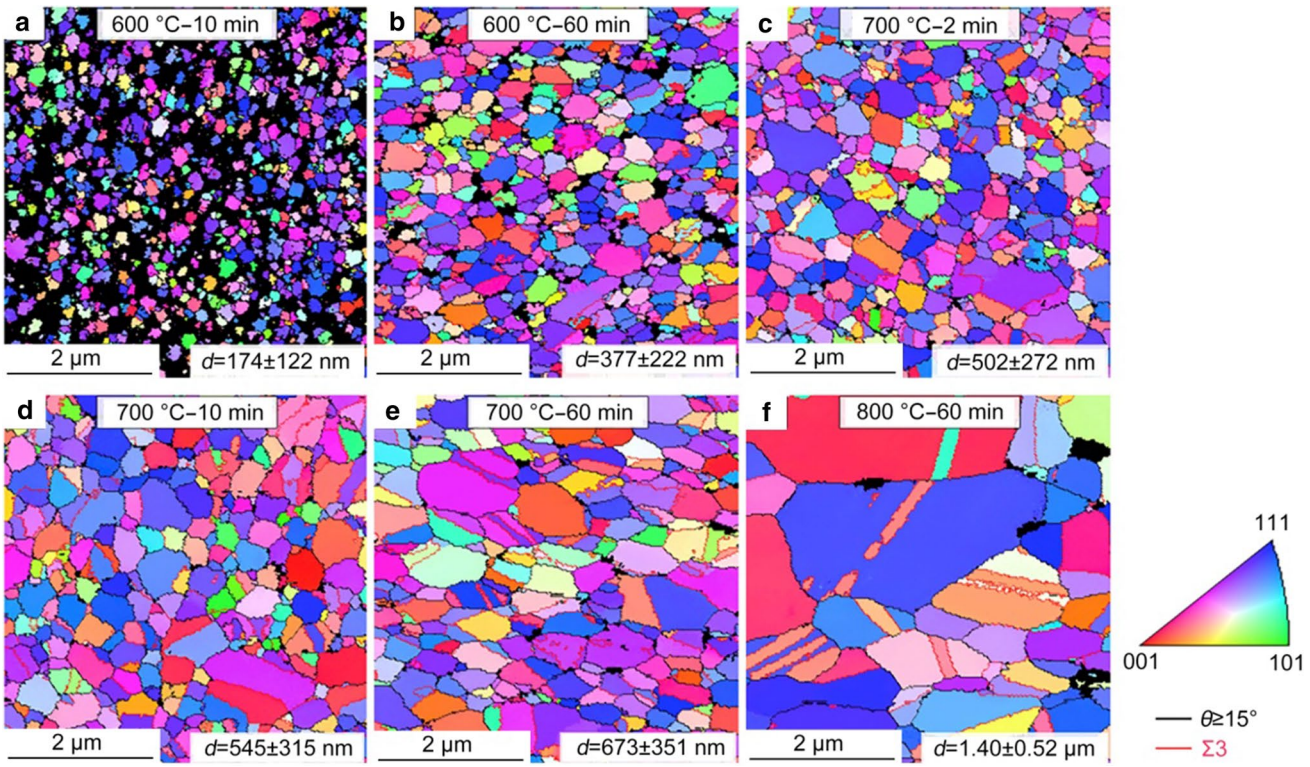

Fig. 13 EBSD-IPF maps of annealed samples after deformation. The color scale on the right corresponds to the inverse pole diagram of [001]. Reproduced with permission from Ref. [63]. Copyright 2020 Elsevier

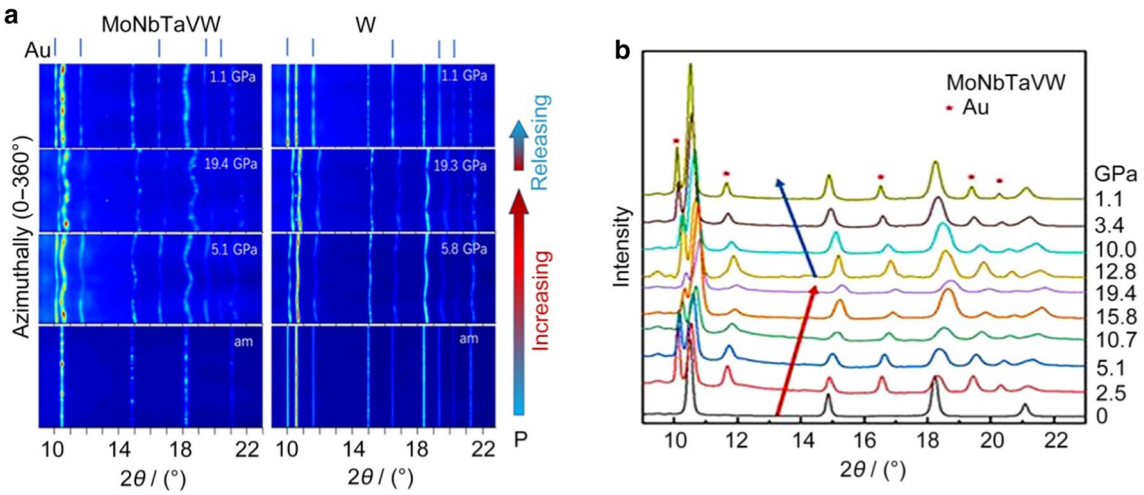

Fig. 14 **a** Azimuthal diffraction images of MoNbTaVW (left) and pure W (right) at different pressures. The diffraction of Au is indicated at the top of the figure. Pressure is marked on the right side of each figure; **b** XRD patterns of the MoNbTaVW/Au mixture during decompression and compression. Reproduced with permission from Ref. [64]. Copyright 2021 Elsevier

Table 3 Chemical compositions (at. %) and Vickers microhardness of intermediate alloy (alloy) and $C_{0.1}$-alloy (C-doped). Reproduced with permission from Ref. [65]. Copyright 2020 MDPI

Sample	C	Mo	Nb	Re	Ta	W	Hardness		
							0.98 N	4.9 N	19.6 N
Alloy	–	14.43 ± 0.17	22.74 ± 0.38	15.29 ± 0.09	26.66 ± 0.19	20.90 ± 0.19	6.451 ± 0.140	6.035 ± 0.303	5.400 ± 0.213
C-doped	0.06	14.32 ± 0.41	22.63 ± 0.54	18.12 ± 0.28	26.44 ± 0.32	18.43 ± 0.26	5.826 ± 0.104	5.905 ± 0.086	5.749 ± 0.203

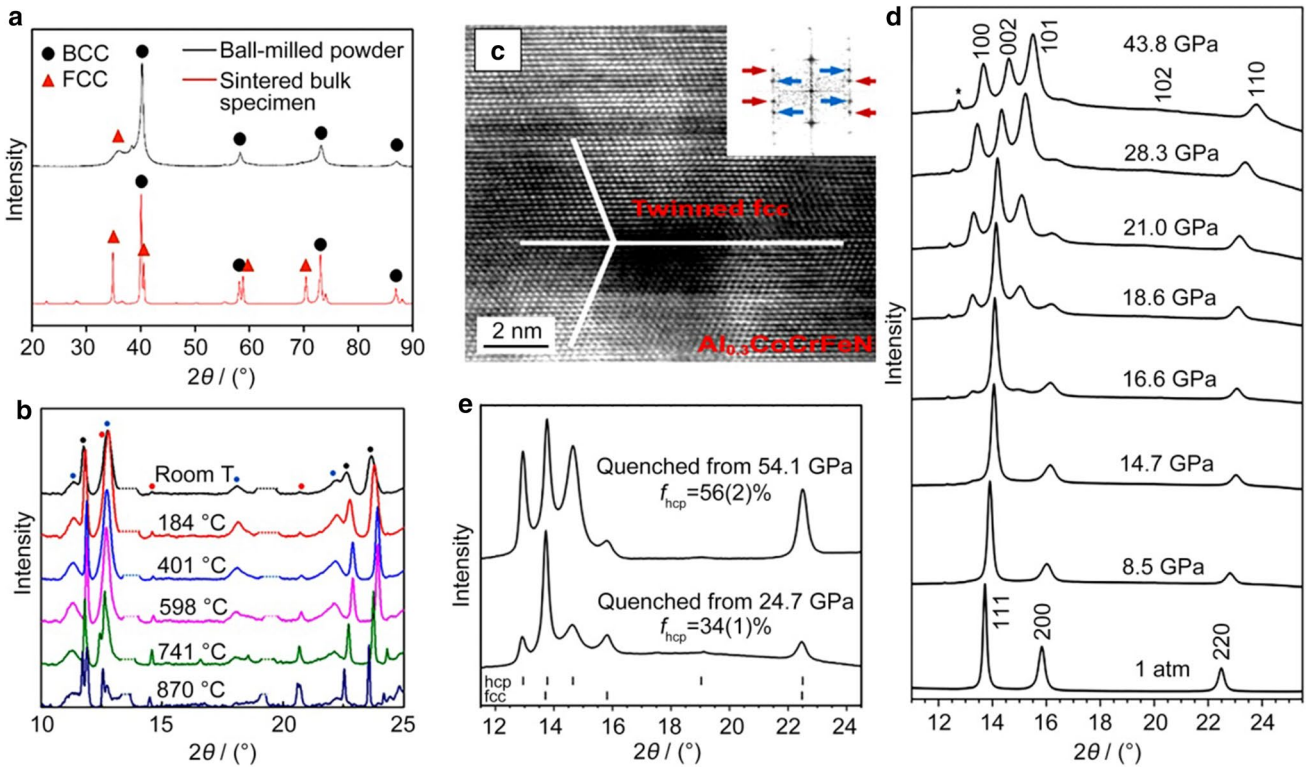

Fig. 15 **a** XRD images of sintered bulk sample (red) and carbon-doped MoNbTaW powder by ball mill method (black); **b** XRD results of C-MoNbTaW/MgO/Pt mixture with different temperatures at 3.1 GPa. Reproduced with permission from Ref. [66]. Copyright 2021 MDPI. **c** HRTEM image of quenched $Al_{0.3}CoCrFeNi$ sample from 53 GPa. Reproduced with permission from Ref. [72]. Copyright 2019 AIP Publishing. **d** XRD patterns of CrMnFeCoNi at different pressures; **e** XRD patterns of quenched CrMnFeCoNi from different pressures. Reproduced with permission from Ref. [74]. Copyright 2017 Springer Nature

temperature to 870 °C at 3.1 GPa. The mechanical properties of C-MoNbTaW were expected to be improved due to the emergence of favorable carbide phases (TaC and NbC) of hard components in the composites.

Yusenko et al. [67] synthesized the fcc-structured $Ir_{0.26}Os_{0.05}Pt_{0.31}Rh_{0.23}Ru_{0.15}$ refractory alloy and studied its compression behavior with DAC technique. The alloy was stable up to 49 GPa at room temperature and the compressibility curve could be fitted with a bulk modulus of 300 (22) GPa, which is little bit smaller than the hcp-$Ir_{0.24}Os_{0.21}Re_{0.16}Rh_{0.18}Ru_{0.20}$ (317(2) GPa) [68]. Ahmad et al. [69] performed XRD experiments on three typical HEAs *fcc*-$Ni_{20}Co_{20}Fe_{20}Mn_{20}Cr_{20}$, bcc-$Hf_{25}Nb_{25}Zr_{25}Ti_{25}$, and hexagonal close-packed (hcp) $Re_{25}Ru_{25}Co_{25}Fe_{25}$ (at.%) under extreme pressure and temperature conditions. The results showed that the three HEAs exhibited great stability up to 80 GPa. The bulk modulus and its pressure derivative of three HEAs were determined and the bcc-$Hf_{25}Nb_{25}Zr_{25}Ti_{25}$ had a relatively larger compressibility than the other two alloys. Yu et al. [70] synthesized HoDyYGdTb HEA and performed high-pressure XRD experiments up to 60.1 GPa at room temperature. The calculated bulk modulus ($B_0 = 45.8$ GPa) and atomic volume ($V_0 = 19.3$ $cm^3 \cdot mol^{-1}$) agreed well with the values calculated by the "additivity law" [71], which is favorable for mechanical properties.

Wang et al. [72] investigated the effect of Al content on the structure of HEAs $Al_xCoCrFeNi$ ($X=0$, 0.1, 0.3, 0.75, 1.5) under high pressure. XRD patterns showed that the structure of $Al_{0.3}CoCrFeNi$ remained stable up to 53 GPa. Moreover, high-resolution TEM (HRTEM) image (Fig. 15c) showed that a new nano-twinned fcc structure was formed, which was proposed as a source of high maximum strength of the alloy [73]. Tracy et al. [74] studied the structure properties of CrMnFeCoNi HEA by angle-dispersive XRD measurements at pressures of up to 54.1 GPa. The results are shown in Fig. 15d. A pressure-induced structure transition from fcc phase to a unique hcp phase was observed starting at 14 GPa. The hcp phase could be quenched to ambient pressure, forming fcc-hcp mixtures. As shown in Fig. 15e, the content of hard hcp phase and ductile fcc phase could be controlled effectively, thus providing a distinctive performance with combined high ductility, strength, and toughness.

6 Conclusion and outlooks

As an emerging alloy material in recent years, HEAs have been at the forefront of advanced metal material research. As a powerful means to study the properties of materials, high-pressure technology brings new possibilities to the properties of HEAs. HPT treatment can be applied to many kinds of HEAs, and the hardness of these alloys can be significantly improved. High-density HEAs and high-entropy nanocomposites were synthesized by HPT treatment, and their hardness was significantly improved. In addition, a combination of good ductility and high strength can be effectively achieved by HPT processing combined with thermal annealing. Besides, the DAC technology combined with XRD technology also provides a way for synthesizing novel structure as well as optimizing the mechanical properties of HEAs.

Although sufficient kinds of HEAs have been developed, only a few of them have been studied under high pressure. In the future, with the help of high-pressure technology, more HEAs will be explored extensively under high pressure. Inspired by the combination of high-pressure technology and thermal annealing treatment, potential properties such as creep under high-pressure high/low-temperature conditions, the dynamic response under high strain rate based on HPT technology, and pressure-directed microstructure optimization (e.g., plasticity-assisted redistribution, grain boundary effect, optimal combination of strength, and plasticity) are worth more exploration in future research.

Acknowledgements This work was supported by the National Natural Science Foundation of China (Grant Nos. 62104090, 11604133, and 11874174), the Natural Science Foundation of Shandong Province (Grant Nos. ZR2017QA013, ZR2021QA087, and ZR2021QA092), the Science and Technology Plan of Youth Innovation Team for Universities of Shandong Province (Grant No. 2019KJJ019), the Introduction and Cultivation Plan of Youth Innovation Talents for Universities of Shandong Province, Fundamental Research Funds for the Central Universities (buctrc 202122), the Research Funding of Liaocheng University (318012016, 318051610, and 318051612), and the Special Construction Project Fund for Shandong Province Taishan Scholars.

Declarations

Conflict of interest The authors declare no conflict of interest.

References

1. Feng R, Zhang CA, Gao MC, Pei ZR, Zhang F, Chen Y, Ma D, An K, Poplawsky JD, Ouyang LZ, Ren Y, Hawk JA, Widom M, Liaw PK. High-throughput design of high-performance lightweight high-entropy alloys. Nat Commun. 2021;12:1.
2. Shi PJ, Li RG, Li Y, Wen YB, Zhong YB, Ren WL, Shen Z, Zheng TX, Peng JC, Liang XL, Hu PF, Min N, Zhang Y, Ren Y, Liaw PK, Raabe D, Wang YD. Hierarchical crack buffering triples ductility in eutectic herringbone high-entropy alloys. Science. 2021;373:912.
3. Yeh JW, Chen SK, Lin SJ, Gan JY, Chin TS, Shun TT, Tsau CH, Chang SY. Nanostructured high-entropy alloys with multiple principal elements: novel alloy design concepts and outcomes. Adv Eng Mater. 2004;6:299.
4. Miracle DB, Senkov ON. A critical review of high entropy alloys and related concepts. Acta Mater. 2017;122:448.
5. Asghari-Rad P, Sathiyamoorthi P, Nguyen NTC, Zargaran A, Kim TS, Kim HS. A powder-metallurgy-based fabrication route towards achieving high tensile strength with ultra-high ductility in high-entropy alloy. Scripta Mater. 2021;190:69.
6. Lee DH, Park JM, Yang GH, He JY, Lu ZP, Suh JY, Kawasaki M, Ramamurty U, Jang J. Nano-graining a particle-strengthened high entropy alloy. Scripta Mater. 2019;163:24.
7. Gubicza J, Hung PT, Kawasaki M, Han JK, Zhao YK, Xue YF, Labar JL. Influence of severe plastic deformation on the microstructure and hardness of a CoCrFeNi high-entropy alloy: a comparison with CoCrFeNiMn. Mater Charact. 2019;154:304.
8. Uporov SA, Ryltsev RE, Sidorov VA, Estemirova SK, Sterkhov EV, Balyakin IA, Chtchelkatchev A. Pressure effects on electronic structure and electrical conductivity of TiZrHfNb high-entropy alloy. Intermetallics. 2022;140:107394.
9. Nguyen NTC, Asghari-Rad P, Sathiyamoorthi P, Zargaran A, Lee CS, Kim HS. Ultrahigh high-strain-rate superplasticity in a nanostructured high-entropy alloy. Nat Commun. 2020;11:1.
10. Guo J, Wang HH, Rohr FV, Wang Z, Cai S, Zhou YZ, Yang K, Li AG, Jiang S, Wu Q, Cava RJ, Sun LL. Robust zero resistance in a superconducting high-entropy alloy at pressures up to 190 GPa. P Natl Acad Sci USA. 2017;50:13144.
11. Zhang WR, Liaw PK, Zhang Y. Science and technology in high-entropy alloys. Sci China Mater. 2018;61:2.
12. Zhang Y, Zou TT, Tang Z, Gao MC, Dahmen KA, Liaw PK, Lu ZP. Microstructures and properties of high-entropy alloys. Prog Mater Sci. 2014;61:1.
13. Lu ZP, Wang H, Chen MW, Baker I, Yeh JW, Liu CT, Nieh TG. An assessment on the future development of high-entropy alloys: summary from a recent workshop. Intermetallics. 2015;66:67.

14. Zhang F, Lou HB, Cheng BY, Zeng ZD, Zeng QS. High-pressure induced phase transitions in high-entropy alloys: a review. Entropy. 2019;21:239.
15. Miracle DB, Miller JD, Senkov ON, Woodward C, Uchic MD, Tiley J. Exploration and development of high entropy alloys for structural applications. Entropy. 2013;16:494.
16. Dong WQ, Zhou Z, Zhang MD, Ma YM, Yu PF, Liaw PK, Li G. Applications of high-pressure technology for high-entropy alloys: a review. Metals. 2019;9:867.
17. Chen TK, Shun TT, Yeh JW, Wong MS. Nanostructured nitride films of multi-element high-entropy alloys by reactive dc sputtering. Surf Coat Tech. 2004;188:193.
18. Hsu CY, Yeh JW, Chen SK, Shun TT. Wear resistance and high-temperature compression strength of fcc $CuCoNiCrAl_{0.5}Fe$ alloy with boron addition. Metall Mater Trans A. 2004;35:1465.
19. Huang PK, Yeh JW, Shun TT, Chen SK. Multi-principal-element alloys with improved oxidation and wear resistance for thermal spray coating. Adv Eng Mater. 2004;6:74.
20. Yeh JW, Chen SK, Gan JY, Lin SJ, Chin TS, Shun TT, Tsau CH, Chang SY. Formation of simple crystal structures in Cu-Co-Ni-Cr-Al-Fe-Ti-V alloys with multiprincipal metallic elements. Metall Mater Trans A. 2004;35:2533.
21. Gludovatz B, Hohenwarter A, Catoor D, Chang EH, George EP, Ritchie RO. A fracture-resistant high-entropy alloy for cryogenic applications. Science. 2014;345:1153.
22. Yeh JW. Recent progress in high entropy alloys. Ann Chim Sci Mat. 2006;31:633.
23. Zhang Y, Zhou YJ, Lin JP, Chen GL, Liaw PK. Solid-solution phase formation rules for multi-component alloys. Adv Eng Mater. 2008;10:534.
24. Zhang Y, Yang X, Liaw PK. Alloy design and properties optimization of high-entropy alloys. Jom. 2012;64:830.
25. Tsai MH, Yeh JW. High-entropy alloys: a critical review. Mater Res Lett. 2014;2:107.
26. Singh S, Wanderka N, Murty BS, Glatzel U, Banhart J. Decomposition in multi-component AlCoCrCuFeNi high-entropy alloy. Acta Mater. 2011;59:182.
27. Tsai KY, Tsai MH, Yeh JW. Sluggish diffusion in Co–Cr–Fe–Mn–Ni high-entropy alloys. Acta Mater. 2013;61:4887.
28. Senkov ON, Wilks GB, Scott JM, Miracle DB. Mechanical properties of $Nb_{25}Mo_{25}Ta_{25}W_{25}$ and $V_{20}Nb_{20}Mo_{20}Ta_{20}W_{20}$ refractory high-entropy alloys. Intermetallics. 2011;19:698.
29. Hsu CY, Juan CC, Wang WR, Sheu TS, Yeh JW, Chen SK. On the superior hot hardness and softening resistance of$AlCoCr_xFeMo_{0.5}Ni$ high-entropy alloys. Mater Sci Eng A. 2011;528:3581
30. Cheng KH, Lai CH, Lin SJ, Yeh JW. Recent progress in multi-element alloy and nitride coatings sputtered from high-entropy alloy targets. Ann Chim. 2006;31:723.
31. Ranganathan S. Alloyed pleasures: multimetallic cocktails. Curr Sci India. 2003;85:1404.
32. Hemley RJ, Ashcroft NW. The revealing role of pressure in the condensed matter sciences. Phys Today. 1998;51:26.
33. Mao HK, Chen B, Chen JH, Li K, Lin JF, Yang W, Zheng HY. Recent advances in high-pressure science and technology. Matter Radiat Extrem. 2016;1:59.
34. Bridgman PW. Effects of high shearing stress combined with high hydrostatic pressure. Phys Rev. 1935;48:825.
35. Zhilyaev AP, Langdon TG. Using high-pressure torsion for metal processing: fundamentals and applications. Prog Mater Sci. 2008;53:893.
36. Edalati K, Horita Z. A review on high-pressure torsion (HPT) from 1935 to 1988. Mater Sci Eng A. 2016;652:325.
37. Valiev RZ, Estrin Y, Horita Z, Langdon TG, Zehetbauer MJ, Zhu YT. Producing bulk ultrafine-grained materials by severe plastic deformation: ten years later. Jom. 2016;68:1216.
38. Bundy FP, Hall HT, Strong HM, Wentorf RH. Man-made diamonds. Nature. 1955;176:51.
39. Bassett WA. Diamond anvil cell, 50th birthday. High Pressure Res. 2009;29:163.
40. Dubrovinsky L, Dubrovinskaia N, Bykova E, Bykov M, Prakapenka V, Prescher C, Glazyrin K, Liermann HP, Hanfland M, Ekholm M, Feng Q, Pourovskii LV, Katsnelson MI, Wills JM, Abrikosov IA. The most incompressible metal osmium at static pressures above 750 gigapascals. Nature. 2015;525:226.
41. Buras B, Olsen JS, Gerward L, Will G, Hinze E. X-ray energy-dispersive diffractometry using synchrotron radiation. J Appl Crystallogr. 1977;10:431.
42. Stepanov ND, Yurchenko NY, Gridneva AO, Zherebtsov SV, Ivanisenko YV, Salishchev GA. Structure and hardness of B2 ordered refractory $AlNbTiVZr_{0.5}$ high entropy alloy after high-pressure torsion. Mater Sci Eng A. 2018;716:308.
43. Sonkusare R, Khandelwal N, Ghosh P, Biswas K, Gurao NP. A comparative study on the evolution of microstructure and hardness during monotonic and cyclic high pressure torsion of CoCuFeMnNi high entropy alloy. J Mater Res. 2019;34:1.
44. Lee DH, Choi IC, Seok MY, He JY, Lu ZP, Suh JY, Kawasaki M, Langdon TG, Jang JI. Nanomechanical behavior and structural stability of a nanocrystalline CoCrFeNiMn high-entropy alloy processed by high-pressure torsion. J Mater Res. 2015;30:2804.
45. Heczel A, Kawasaki M, Labar JL, Jang JI, Langdon TG, Gubicza J. Defect structure and hardness in nanocrystalline cocrfemnni high-entropy alloy processed by high-pressure torsion. J Alloy Compd. 2017;711:143.
46. Edalati P, Mohammadi A, Ketabchi M, Edalati K. Ultrahigh hardness in nanostructured dual-phase high-entropy alloy AlCrFeCoNiNb developed by high-pressure torsion. J Alloy Compd. 2021;884:161101.
47. Yu PF, Cheng H, Zhang LJ, Zhang H, Jing Q, Ma MZ, Liaw PK, Li G, Liu RP. Effects of high pressure torsion on microstructures and properties of an $Al_{0.1}CoCrFeNi$ high-entropy alloy. Mater Sci Eng A. 2016;655:283.
48. Edalati K, Li HW, Kilmametov A, Floriano R, Borchers C. High-pressure torsion for synthesis of high-entropy alloys. Metals. 2021;11:1263.
49. Taheriniya S, Davani FA, Hilke S, Hepp M, Gadelmeier C, Chellali MR, Boll T, Rosner H, Peterlechner M, Gammer C, Divinski SV, Butz B, Glatzel U, Hahn H, Wilde G. High entropy alloy nanocomposites produced by high pressure torsion. Acta Mater. 2021;208:116714.
50. Tang QH, Huang Y, Huang YY, Liao XZ, Langdon TG, Dai PQ. Hardening of an $Al_{0.3}CoCrFeNi$ high entropy alloy via high-pressure torsion and thermal annealing. Mater Lett. 2015;151:126.
51. Kilmametov A, Kulagin R, Mazilkin A, Seils S, Boll T, Heilmaier M, Hahn H. High-pressure torsion driven mechanical alloying of cocrfemnni high entropy alloy. Scripta Mater. 2019;158:29.
52. Schuh B, Mendez-Martin F, Volker B, George EP, Clemens H, Pippan R, Hohenwarter A. Mechanical properties, microstructure and thermal stability of a nanocrystalline CoCrFeMnNi high-entropy alloy after severe plastic deformation. Acta Mater. 2015;96:258.
53. Kawasaki M, Langdon TG. Principles of superplasticity in ultrafine-grained materials. J Mater Sci. 2007;42:1782.
54. Langdon TG. Seventy-five years of superplasticity: historic developments and new opportunities. J Mater Sci. 2009;44:5998.
55. Shahmir H, He JY, Lu ZP, Kawasaki M, Langdon TG. Evidence for superplasticity in a CoCrFeNiMn high-entropy alloy processed by high-pressure torsion. Mater Sci Eng A. 2017;685:342.
56. Nguyen NTC, Moon J, Sathiyamoorthi P, Asghari-Rad P, Kim GH, Lee CS, Kim HS. Superplasticity of $V_{10}Cr_{15}Mn_5Fe_{35}Co_{10}Ni_{25}$ high-entropy alloy processed using high-pressure torsion. Mater Sci Eng A. 2019;764:138198.

57. Ma E, Wu XL. Tailoring heterogeneities in high-entropy alloys to promote strength–ductility synergy. Nat Commun. 2019;10:1.
58. Sathiyamoorthi P, Kim HS. High-entropy alloys with heterogeneous microstructure: processing and mechanical properties. Prog Mater Sci. 2020;2:100709.
59. Li WD, Xie D, Li DY, Gao YF, Liaw PK. Mechanical behavior of high-entropy alloys. Prog Mater Sci. 2021;2:100777.
60. Pan QS, Zhang LX, Feng R, Lu QH, An K, Chuang AC, Poplawsky JD, Liaw PK, Lu L. Gradient cell–structured high-entropy alloy with exceptional strength and ductility. Science. 2021;2:8114.
61. Valiev RZ, Sergueeva AV, Mukherjee AK. The effect of annealing on tensile deformation behavior of nanostructured SPD titanium. Scripta Mater. 2003;49:669.
62. Shahmir H, He JY, Lu ZP, Kawasaki M, Langdon TG. Effect of annealing on mechanical properties of a nanocrystalline CoCrFeNiMn high-entropy alloy processed by high-pressure torsion. Mater Sci Eng A. 2016;676:294.
63. Asghari-Rad P, Sathiyamoorthi P, Nguyen NTC, Bae JW, Shahmir H, Kim HS. Fine-tuning of mechanical properties in $V_{10}Cr_{15}Mn_5Fe_{35}Co_{10}Ni_{25}$ high-entropy alloy through high-pressure torsion and annealing. Mater Sci Eng A. 2020;771:138604.
64. Zhang CY, Yue BB, Bhandari U, Starovoytov ON, Yang Y, Ypung DP, Yan JY, Hong F, Yang SZ. In situ study on the compression deformation of MoNbTaVW high-entropy alloy. J Alloy Compd. 2021;871:159557.
65. Zhang CY, Bhandari U, Zeng CY, Ding H, Guo SM, Yan JY, Yang SZ. Carbide formation in refractory $Mo_{15}Nb_{20}Re_{15}Ta_{30}W_{20}$ alloy under a combined high-pressure and high-temperature condition. Entropy. 2020;22:718.
66. Zhang CY, Bhandari U, Lei JL, Zeng CY, Guo SM, Choi H, Nam S, Yan JY, Yang SZ, Gao F. Performance of carbide alloy compounds in carbon doped MoNbTaW. Curr Comput-Aided Drug Des. 2021;11:1073.
67. Yusenko KV, Khandarkhaeva S, Fedotenko T, Pakhomova A, Gromilov SA, Dubrovinsky L, Dubrovinskaia N. Equations of state of rhodium, iridium and their alloys up to 70 GPa. J Alloy Compd. 2019;788:212.
68. Yusenko KV, Riva S, Carvalho PA, Yusenko MV, Arnaboldi S, Sukhikh AS, Hanfland M, Gromilov SA. First hexagonal close packed high-entropy alloy with outstanding stability under extreme conditions and electrocatalytic activity for methanol oxidation. Scripta Mater. 2017;138:22.
69. Ahmad AS, Su Y, Liu SY, Stahl K, Wu YD, Hui XD, Ruett U, Gutowski O, Glazyrin K, Liermann HP, Franz H, Wang H, Wang XD, Cao QP, Zhang DX, Jiang JZ. Structural stability of high entropy alloys under pressure and temperature. J Appl Phys. 2017;121:235901.
70. Yu PF, Zhang LJ, Ning JL, Ma MZ, Zhang XY, Li YC, Liaw PK, Li G, Liu RP. Pressure-induced phase transitions in HoDyYGdTb high-entropy alloy. Mater Lett. 2017;196:137.
71. Fakirov S. On the application of the "rule of mixture" to microhardness of complex polymer systems containing a soft component and/or phase. J Mater Sci. 2007;42:1131.
72. Wang CX, Tracy CL, Park S, Liu J, Ke F, Zhang FX, Yang TF, Xia SQ, Li CY, Wang YG, Zhang Y, Mao WL, Ewing RC. Phase transformations of Al-bearing high-entropy alloys $Al_xCoCrFeNi$ (x= 0, 0.1, 0.3, 0.75, 1.5) at high pressure. Appl Phys Lett. 2019;114:091902.
73. Li XY, Wei YJ, Lu L, Lu K, Gao HJ. Dislocation nucleation governed softening and maximum strength in nano-twinned metals. Nature. 2010;464:877.
74. Tracy CL, Park S, Rittman DR, Zinkle SJ, Bei HB, Lang M, Ewing RC, Mao WL. High pressure synthesis of a hexagonal close-packed phase of the high-entropy alloy CrMnFeCoNi. Nat Commun. 2017;8:1.